nature physics
SUPPLEMENTARY INFORMATION
DOI: 10.1038/NPHYS3634

SUPPLEMENTARY INFORMATION: CRITICAL SPIN FLUCTUATIONS AND THE ORIGIN OF NEMATIC ORDER IN $Ba(Fe_{1-x}Co_x)_2As_2$

I. DETERMINATION OF THE SPOT TEMPERATURE

In Fig. 2 of the main text and Figs. S2 and S3 we show that the response from fluctuations is maximal at T_s and then decreases. For $x = 0$ the decrease is very rapid, at $x = 0.025$ and 0.051 the fluctuations disappear only below $T_{\rm SDW}$. Since $\Delta T = T_s - T_{\rm SDW}$ is small close to zero doping, the laser-induced heating has to be determined precisely. In addition, a large temperature gradient in the spot would lead to a substantial reduction of the maximal fluctuation intensity. Great care was therefore taken to keep the temperature gradient in the spot small and to determine the spot temperature and to calibrate it against intrinsic thermometers. The calibration is possible since twin boundaries develop below T_s in the samples with $x = 0.025$ and 0.051 facilitating a very precise determination of T_s. First we studied the effect of increasing laser power P_L at different holder temperatures T_h on the twin pattern that can be seen, e.g., in Fig. S1 c1. In this way the laser heating ΔT_L was determined to be $1 \pm 0.1\,\mathrm{K/mW}$ for a spot diameter $d = 50\,\mu$m. (Note that ΔT_L scales as d^{-1} and not as d^{-2}.) Next we heat the sample slowly through T_s using $P_L = 0.3\,$mW as shown in a series of snapshots in Fig. S1 c1–c6. The twin boundaries appear as horizontal lines and are most pronounced in (c1). With increasing temperature they "melt" and finally disappear completely at 102.9 K (extrapolated sample temperature for $P_L = 0$), and we identify $T_s = 102.9\,$K. The transition can be observed very clearly in movie M1.

For estimating $T_{\rm SDW}$ we analyze the phonons. The A_{1g} As vibration was reported to appear in B_{2g} symmetry below T_s[1]. (We maintain the tetragonal 2 Fe unit cell here as opposed to the main text to avoid confusion with the usual phonon assignment. In the proper orthorhombic 4 Fe unit cell applying below $T_{\rm SDW}$ the phonon switches to A_g symmetry, and B_{2g} symmetry is not accessible any further with in-plane polarizations.) Our precise temperature determination shows for $x = 0.025$ that the anomalous intensity does not appear at T_s. Rather the phonon anomaly appears only at approximately 97 K as shown in Fig. S1 b. According to the phase diagram the magnetic transition is offset by approximately 4-5 K at $x = 0.025$. This is actually not unexpected for a phonon that is not coupled to the lattice distortion by symmetry[2]. By measuring the B_{2g} intensity of the A_{1g} phonon we can

DOI: 10.1038/NPHYS3634

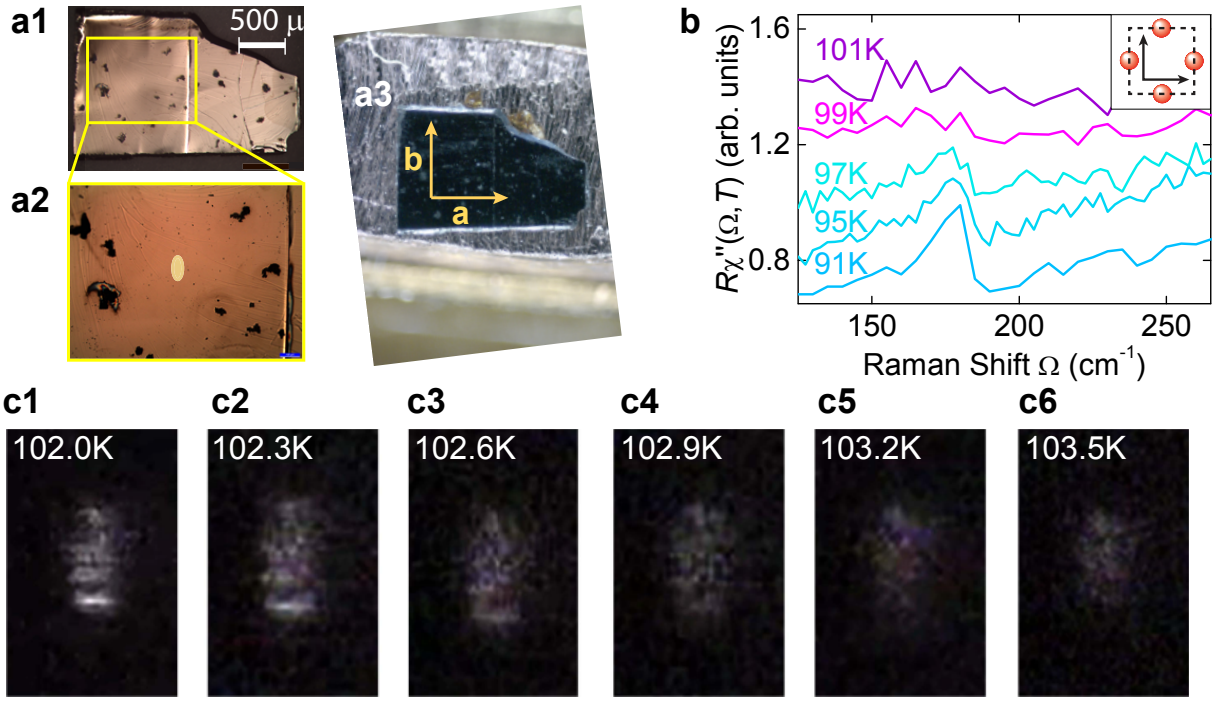

FIG. S1. Determination of the spot temperature. **a1** and **a2** show the sample surface and a zoom in thereof. In **a2** the approximate laser spot is indicated schematically. **a3** shows the crystallographic axes of the tetragonal phase. **b** A_g phonon around T_{SDW}. Above T_{SDW} the symmetry leakage of the phonon is negligibly small. Only below T_{SDW} the intensity becomes appreciable. **c** Image of the illuminated spot as a function of temperature. The horizontal lines in **c1**–**c3** result from twin boundaries. In addition to the appearance of twin boundaries the reversible adsorption of residual gas atoms and molecules starts instantaneously and enhances the stray-light in the spot. See also movie M1.

therefore identify the magnetic transition temperature and find $T_{\mathrm{SDW}} = 98 \pm 1\,\mathrm{K}$.

For $x = 0.051$ we find $T_s = 61.0 \pm 0.2\,\mathrm{K}$ and $T_{\mathrm{SDW}} = 50 \pm 2\,\mathrm{K}$. Here, the A_{1g} phonon appears already above T_{SDW}, and we identify T_{SDW} with the strongest increase of the intensity. In addition, we know the width of the nematic phase from the phase diagram[3] (Fig. 5) and find an anomaly of $\Gamma_{0,\mu}(T)$ close to T_{SDW} [see Fig. S4 d]. Hence the relevant temperatures are known with high precision.

II. RESULTS AT $x = 0$ AND $x = 0.051$

Figs. S2 and S3 show the experimental results for $x = 0$ and $x = 0.051$. At $x = 0$ the two transitions $T_{\rm SDW}$ and T_s either coincide or are too close to be observed separately while the response of the SDW phase can be identified clearly as observed earlier[4,5]. At $x = 0.051$ the fluctuations can be separated out in the usual way as described below. If an extraction is attempted in a similar way at $x = 0.085$ the variation with temperature cannot be described with Aslamazov-Larkin-type of fluctuations. Although the response increases slightly towards lower temperature[6] and the elastic constants may still indicate an instability up to 9% Co substitution[7] we do not feel comfortable to extract parameters in this case. The results for $\Gamma_{0,\mu}(T)$ are compiled in Fig. S4.

III. MEMORY FUNCTION AND STATIC RELAXATION RATES

In Fig. 2 d symmetry-dependent static relaxation rates $\Gamma_{0,\mu}(T)$ are shown for $\mu = A_{1g}$ and B_{1g},

$$\frac{\hbar}{\tau_{0,\mu}(T)} = \Gamma_{0,\mu}(T) = \left(\frac{\partial R\chi''_\mu(\Omega,T)}{\partial\Omega}\right)^{-1}\Bigg|_{\Omega=0}. \tag{S1}$$

Since the overall intensity of the spectra is not known in absolute units the experimental constant R, to which the initial slope $\tau_{0,\mu}(T)$ is proportional, cannot be pinned down. If one is interested in energy units for $\Gamma_{0,\mu}(T)$ one needs additional information except for the case of electron scattering off impurities[8] where the energy of the intensity maximum reflects $\Gamma_{0,\mu}(T)$. In all other cases $\Gamma_{0,\mu}(T)$ must be extracted from $\Gamma_\mu(\Omega,T)$ for facilitating a comparison to transport data. This problem was solved a while ago by adopting the memory function method[9,10] for Raman scattering[11]. Then $\Gamma_{0,\mu}(T)$ can be derived by extrapolating the dynamic Raman relaxation rates $\Gamma_\mu(\Omega,T) = \hbar/\tau_\mu(\Omega,T)$. The results for all doping levels are compiled in Fig. S4.

If a Drude model is applied the resistivities $\rho(T)$ can be converted into static scattering rates. Using a plasma frequency close to 1 eV in rough agreement with optical data[12], the analysis shows that the Raman and transport results are compatible above a doping dependent temperature T_f that is identified here with the onset of fluctuations in agreement with results from other methods. Transport and Raman scattering agree to within the experimental precision, possibly indicating the common origin of the electronic relaxation on the electron and hole bands.

DOI: 10.1038/NPHYS3634

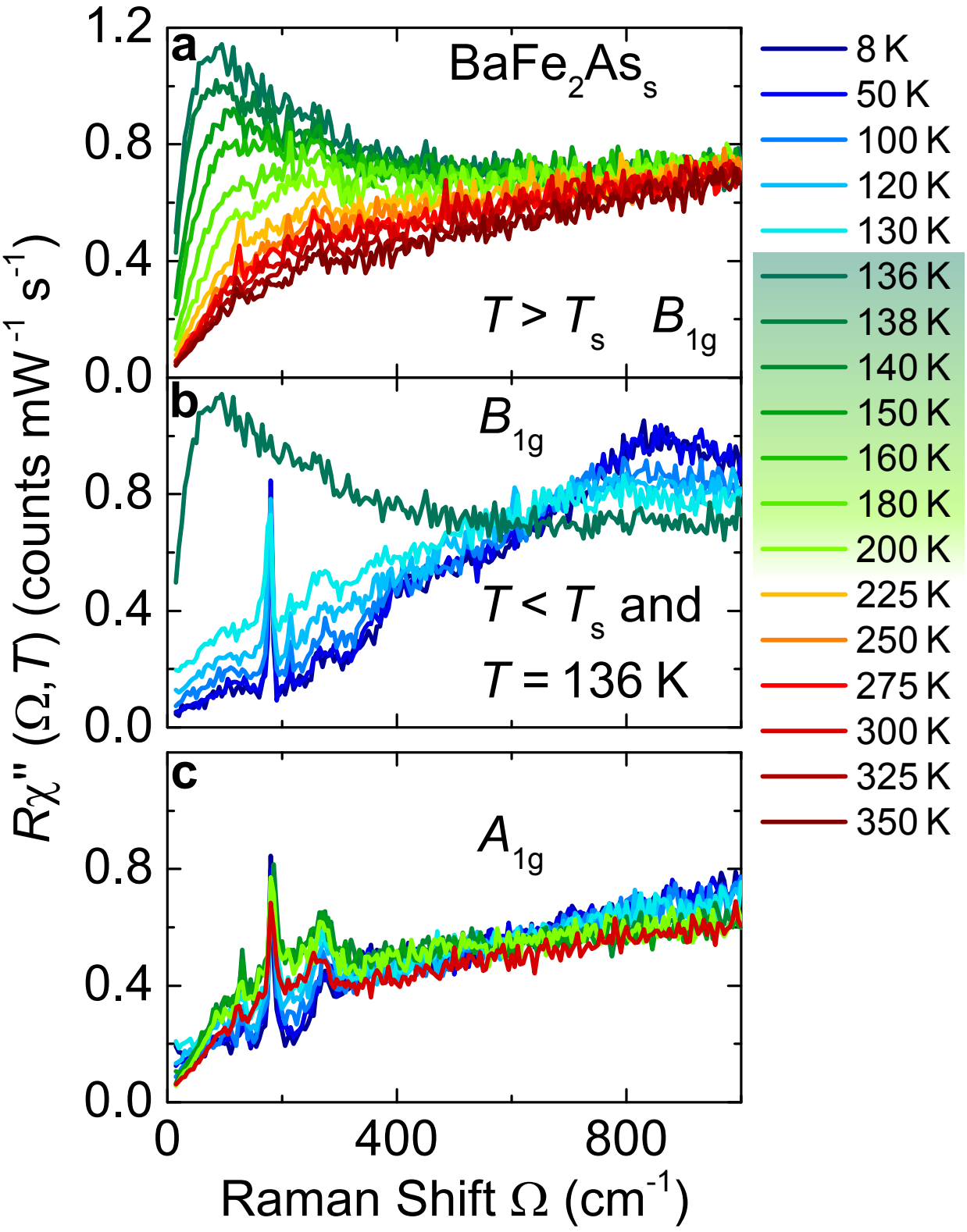

FIG. S2. Raman response $R\chi''(\Omega, T)$ (raw data) of $BaFe_2As_2$ in **a**, **b** B_{1g} and **c** A_{1g} symmetry above and below the structural transition T_s at temperatures as indicated.

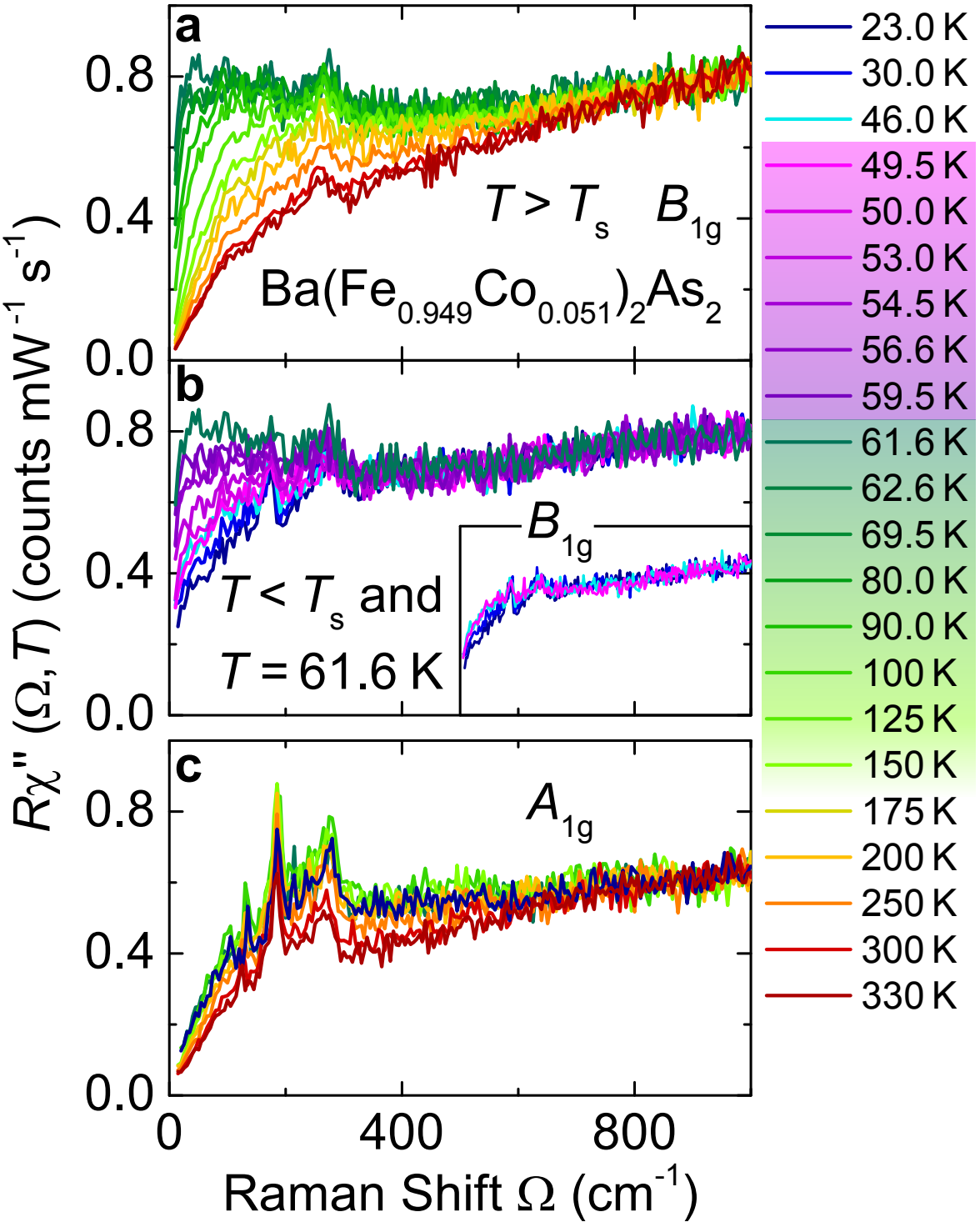

FIG. S3. Raman response $R\chi''(\Omega, T)$ (raw data) of $Ba(Fe_{0.949}Co_{0.051})_2As_2$ in **a**, **b** B_{1g} and **c** A_{1g} symmetry above and below the structural transition T_s at temperatures as indicated. The inset in **b** shows that the SDW gap starts opening within 5 K below T_{SDW}.

DOI: 10.1038/NPHYS3634

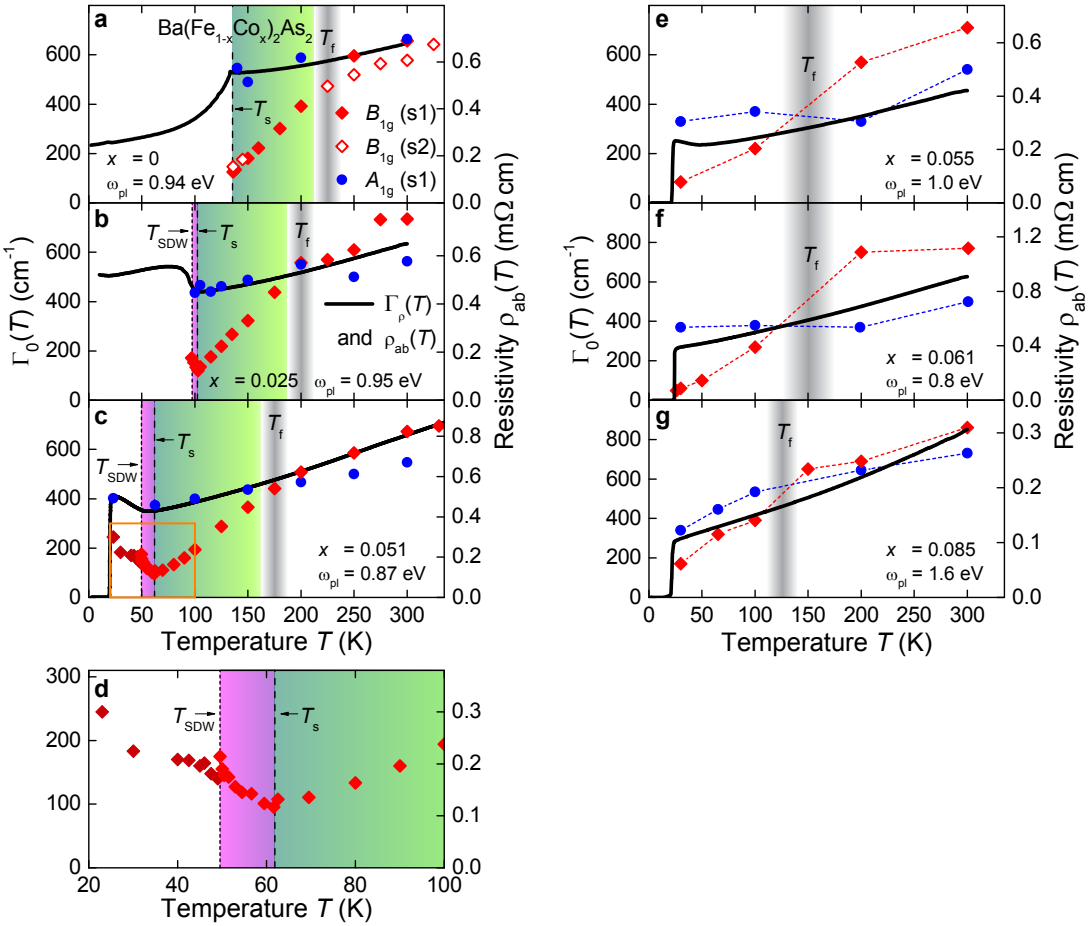

FIG. S4. Static Raman relaxation rates $\Gamma_{0,\mu}(T)$ of $Ba(Fe_{1-x}Co_x)_2As_2$ at **a** $x = 0$, **b**, $x = 0.025$, **c** and **d** $x = 0.051$, **e** $x = 0.055$, **f** $x = 0.061$, and **g** $x = 0.085$. $\Gamma_{0,\mu}(T)$ is derived formally via the memory function method[11] as described in section III. Above the onset temperature of the fluctuations T_f the results in both A_{1g} (blue) and B_{1g} (red) symmetry return results similar to those from the resistivity[3] (right ordinate). Using a Drude model, the resistivities $\rho(T)$ can be converted into scattering rates. At T_f the temperature dependence in the B_{1g} symmetry becomes much stronger. **d** If the resolution in temperature is very high, one finds anomalies of $\Gamma_{0,\mu}(T)$ at T_s and $T_{\rm SDW}$ which facilitates the independent determination of T_s and $T_{\rm SDW}$ directly from the electronic Raman spectra.

IV. ASLAMAZOV-LARKIN DIAGRAMS AND SELECTION RULES

The coupling of visible light to critical fluctuations with wavevectors $|\mathbf{q_c}| = \mathbf{Q} > \mathbf{0}$ and energy (mass) ω_m is possible only via the creation of two excitations with opposite

momenta warranting zero net momentum transfer applying for photon energies in the eV range [Fig. S5 a]. This process can be described by Aslamazov-Larkin (AL) diagrams[13]. We assume a simplified model of the Fermi surface. The central sheet is a circular hole-like pocket around the Γ point [grey circle in Fig. S5 b]. The two electron-like elliptical pockets with the principle axes rotated by 90° are centered at the X $(\pm\pi, 0)$ and Y $(0, \pm\pi)$ points of the 1 Fe BZ. If they are backfolded they intersect with the central hole band as indicated by yellow circle in [Fig. S5 b]. The fluctuation contribution to the Raman spectrum has been analyzed by Caprara and coworkers for the cuprates[13] and arises from the AL diagrams shown in Fig S5 a. The selection rules can be deduced by considering cancelation effects arising from different hot-spots within the fermionic loop as shown in Fig. S5 a. Even if the entire Fermi surface is taken into account the selection rules still work in the Fe-based materials. For instance, in either case full cancellation is found for B_{2g} symmetry[14].

Explicitly written out, the fermionic loop is given by[13–16]

$$\begin{aligned}
\theta_{i,\mu}(\mathbf{q}_c, \Omega, \omega_m) &= \theta^{(1)}_{i,\mu}(\mathbf{q}_c, \Omega, \omega_m) + \theta^{(2)}_{i,\mu}(\mathbf{q}, \Omega, \omega_m), \\
\theta^{(1)}_{i,\mu}(\mathbf{q}_c, \Omega, \omega_m) &= T\sum_n \int_{\mathbf{k}} \gamma^{\mu}_{\mathbf{k}} G_\Gamma(\mathbf{k}, \varepsilon_n - \Omega) G_\Gamma(\mathbf{k}, \varepsilon_n) G_i(\mathbf{k} - \mathbf{q}_c, \varepsilon_n - \omega_m), \\
\theta^{(2)}_{i,\mu}(\mathbf{q}_c, \Omega, \omega_m) &= T\sum_n \int_{\mathbf{k}} \gamma^{\mu}_{\mathbf{k}} G_i(\mathbf{k}, \varepsilon_n - \Omega) G_i(\mathbf{k}, \varepsilon_n) G_\Gamma(\mathbf{k} - \mathbf{q}_c, \varepsilon_n - \Omega + \omega_m),
\end{aligned} \tag{S2}$$

where $\gamma^{\mu}_{\mathbf{k}}$ is the form factor ($\mu = B_{1g},\ A_{1g}$ etc.), and G_i is the electron propagator on band $i = \Gamma,\ X,\ Y$. ε_n is the electronic energy and Ω is the energy difference between the incoming and scattered photons. Experimentally, pure symmetries can be obtained from linear combinations of the response measured at appropriate polarizations of the incoming and scattered photons $\hat{e}_i$ and $\hat{e}_s$.

For illustration purposes the fermionic loop θ is approximated in the hot-spot approximation. Hot-spots are regions in momentum space where both $\mathbf{k}$ and $\mathbf{k} \pm \mathbf{q_c}$ lie on the Fermi surface [Fig S5 b]. Since the loop θ contains the symmetry factor $\gamma(\mathbf{k})$ linearly inside the momentum integral the sign of $\gamma(\mathbf{k})$ is crucial. If $\gamma(\mathbf{k})$ changes sign for different hot spots connected by $\mathbf{q_c}$ (Fig. S5 c, d, and e for A_{1g}, B_{1g}, B_{2g}, respectively) there will be full or partial cancelation within θ. Full cancelation is observed for the first two (and also higher) orders of B_{2g} symmetry [Fig. S5 e]. In contrast, $\gamma(\mathbf{k})$ does not change sign across different hot-spots for the B_{1g} channel. Consequently, in B_{1g} and B_{2g} the fluctuations are Raman active and inactive, respectively.

DOI: 10.1038/NPHYS3634

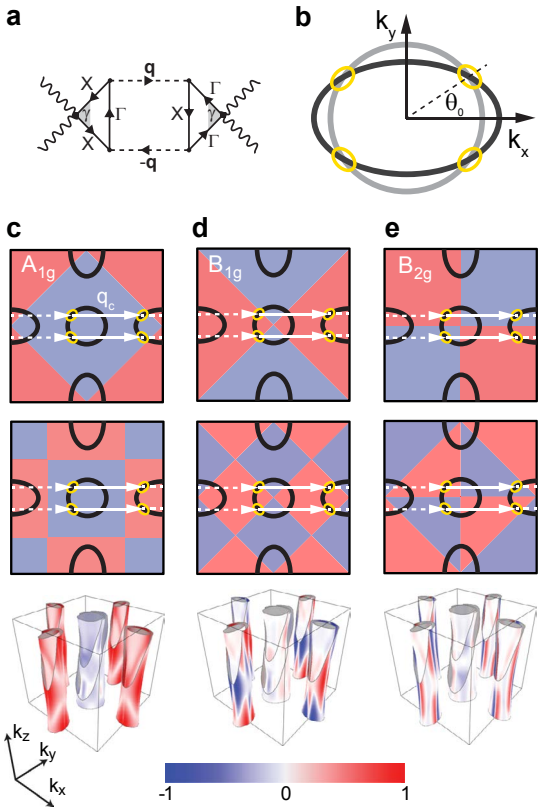

FIG. S5. Scattering from fluctuations. **a** Example of an Aslamazov-Larkin diagram describing light scattering from critical fluctuations with momentum $\pm\mathbf{q_c}$ and energy ω_m. All four diagrams are shown in Ref. 17. The dashed lines represent the magnetic fluctuations, the full lines the fermionic propagators. **b** Hole- (grey) and back-folded electron-like (black) Fermi surfaces intersecting in the hot-spots (yellow circles). The selection rules can be deduced by considering cancelation effects arising from different hot-spot contributions inside the fermionic loops described in Eq. (S2). The first and second row of **c**, **d** and **e** show the signs and nodes of the first and second order A_{1g}, B_{1g}, and B_{2g} Brillouin zone harmonics that indicate where cancellation effects can and cannot be expected. The $\mathbf{q_c}$ vectors for $(\pi, 0)$ and equivalent fluctuations are indicated by full and broken arrows, respectively. The last row shows the vertices derived from the second derivative of tight-binding band structure (effectice mass approximation) of Graser *et al.* (Ref. 18). These vertices provide the best estimate for the sensitivity on the Fermi surface[19]. The A_{1g} vertices for the hole and the electron bands are predominantly negative (blue) and positive (red), respectively. The effective mass approximation shows that the A_{1g} response will be dominated by the second order vertex $\cos k_x \cos k_y$ rather than the lowest order one as already pointed out in Ref. 20.

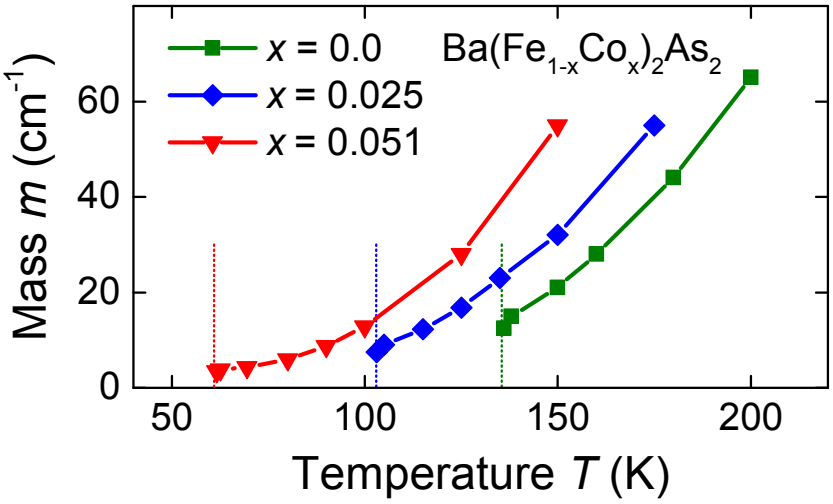

FIG. S6. Mass of the fluctuation propagator $m(x,T) \propto \xi_m^{-2}$ at doping levels x as indicated. The structural transition temperatures are represented by dashed vertical lines.

The A_{1g} symmetry is more complicated in that the first order contribution, proportional to $\cos(k_x) + \cos(k_y)$ [upper row of Fig. S5 c] as used in Ref. 21 on pure symmetry grounds, would be as strong as the B_{1g} contribution [Fig. S5 d] whereas the second order contribution $(\cos(k_x)\cos(k_y))$ [second row of Fig. S5 c] shows cancelation. For clarifying the relative magnitude of the two orders we analyze the effective mass vertices on the Fermi surfaces (second derivative or curvature of the band structure), that are the best approximations for the sensitivity away from resonances, in a way similar to what was proposed in Ref. 20. The last row of Fig. S5 c shows that the band curvatures corresponding to the A_{1g} vertex

$$\gamma_{i,A1g}(\mathbf{k}) = \frac{\partial^2 \varepsilon_{i,\mathbf{k}}}{\partial k_x \partial k_x} + \frac{\partial^2 \varepsilon_{i,\mathbf{k}}}{\partial k_y \partial k_y} \tag{S3}$$

on the Fermi surface of the hole and the electron bands (i) are predomininantly negative and positive, respectively, as expected already for simple parabolic bands with masses $m_h \approx -m_e$ although there are various near nodes on both bands. This result shows that $\cos(k_x)\cos(k_y)$ is the leading order. We note that $\cos(k_x)\cos(k_y)$ predicts a stronger mixing of the particle-hole response from the electron and hole bands than $\cos(k_x) + \cos(k_y)$ as already outlined by Mazin *et al.* in Ref. 20.

V. FITTING PARAMETERS

For fitting the fluctuation response (Fig. 2 of the main text and Fig. S7) we use the

DOI: 10.1038/NPHYS3634

expressions derived in Ref. [13]. For temperatures above T_s we fit the data at a single temperature using the overall intensity, being proportional to $\theta_{i,\mu}(\mathbf{q}_c, \Omega, \omega_m)$ [see Eq. S2], and the mass $m(x,T)$ of the Ornstein-Zernike fluctuation propagator as free parameters. The form of the propagator is close to what is found by neutron scattering[22], and the mass is related to the magnetic correlation length ξ_m as $m(x,T) \propto \xi_m^{-2}$. For the spectra at all other temperatures $T > T_s$ the mass is the only fitting parameter. As shown in Fig. S6, it decreases by and large linearly at high temperature as expected for thermal fluctuations but saturates at finite temperature and energy since the magnetic correlation length does not diverge at T_s. Below T_s the mass is kept fixed at $m(x,T_s)$ and $\theta_{i,\mu}(\mathbf{q}_c, \Omega, \omega_m)$ is varied so as to reproduce the intensity properly. As can be seen from Fig. 2 of the main text, the fluctuations seen in the Raman response saturate at the structural transition, i.e. before ξ_m diverges at T_{SDW}. The comparison to results from other experiments was done already earlier by Gallais et al.[6]. However, we find a nice correspondence between the magnitude of the electronic nematic susceptibility and the elasitic constant m_{66} of $Ba(Fe_{1-x}Co_x)_2As_2$ found by Kuo et al.[23].

VI. INITIAL SLOPE

For being a causal function the Raman response is antisymmetric and, as long as there is no gap, linear around the origin. Then Eq. (S1) can be approximated as

$$\begin{aligned}\tau_{0,\mu}(T) &= \left(\frac{\partial R\chi''_\mu(\Omega,T)}{\partial\Omega}\right)\Big|_{\Omega=0} \\ &= \lim_{\Omega\to 0}\left(\frac{R\chi''_\mu(\Omega,T)}{\Omega}\right). \end{aligned} \tag{S4}$$

The temperature dependence (not the magnitude) of the initial slope can then directly be read off a graph if the response is divided by the energy Ω and plotted against a logarithmic energy scale.

If R was known $\tau_0(T)$ could be determined directly. With R unknown only the relative change can be derived in this way. Fig. S7 shows that the fits reproduce the overall data rather well at low energy. The phenomenological curves can be extended to arbitrarily low energies providing a simple way to directly visualize the temperature dependence of $\tau_0(T)$. Fig. S7 shows also that the experimental data close to zero energy are not very stable. This problem arises from accumulating surface layers and the influence of the laser line.

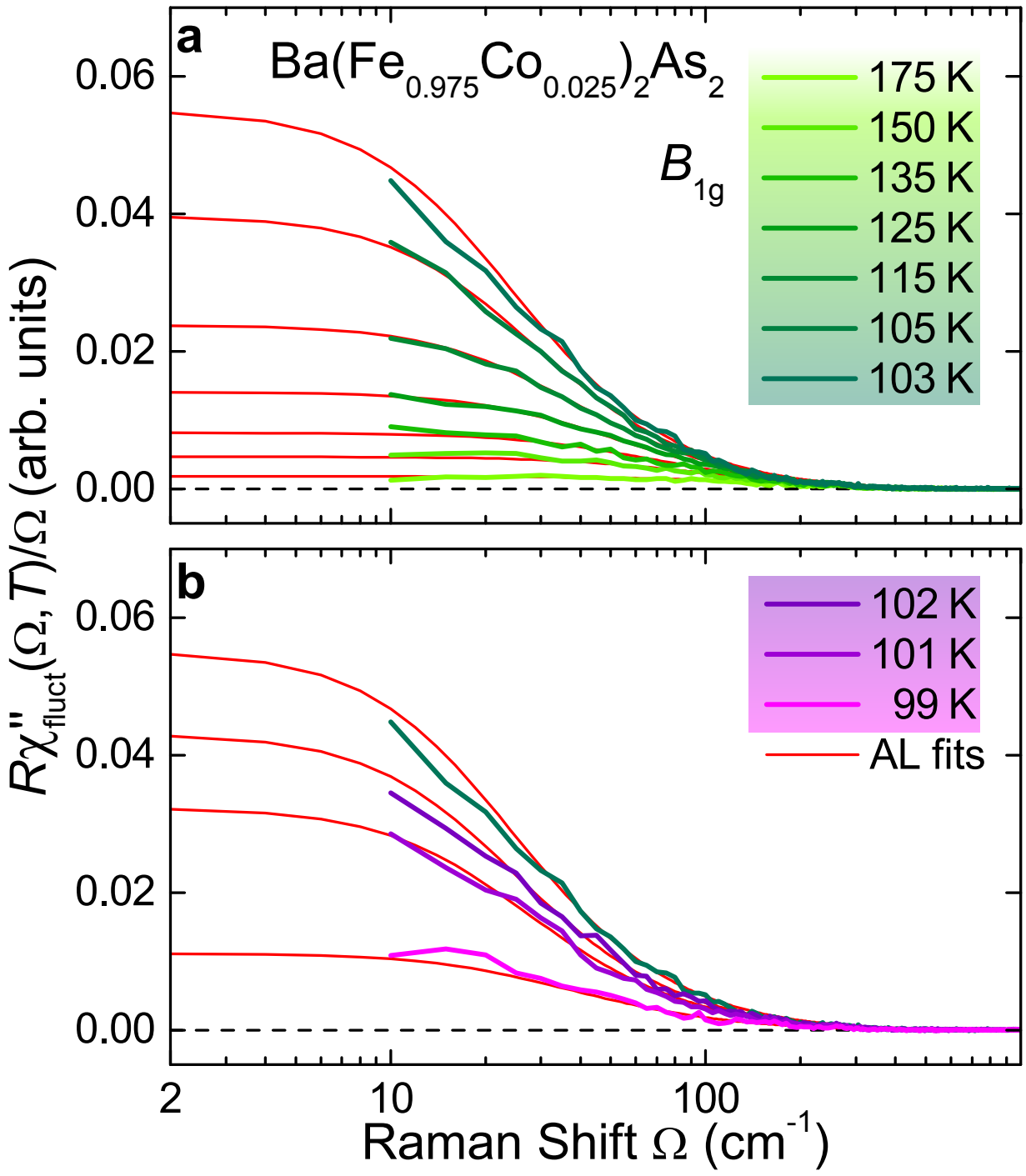

FIG. S7. Initial slope of the Raman response of $Ba(Fe_{1-x}Co_x)_2As_2$ ($x = 0.025$) below T_f. This figure is a reproduction of Fig. 2 with the fluctuation response divided by the energy Ω plotted against a logarithmic energy scale.

DOI: 10.1038/NPHYS3634

Therefore, the error bars become excessively large if the slope is directly extracted from the data. Here we use a wide spectral range to improve the reproducibility.

VII. SUBTRACTION OF THE CONTINUUM

The fluctuation response is superposed on the particle-hole continuum that essentially reflects symmetry-resolved transport properties[19]. Since the contribution of the fluctuations is relatively strong here they can be isolated with little uncertainty. The simplest way is to use the continuum at or slightly above the crossover temperature T_f and subtract it from all spectra measured below T_f. This was sufficient for $ErTe_3$[24] but created negative intensities in the case of $La_{2-x}Sr_xCuO_4$[25].

Here, we wish to compare the temperature dependence of the fluctuations to a theoretical prediction and have to improve on the subtraction of the continuum. To this end we make the analytical phenomenology for the B_{1g} continuum temperature dependent in a way that yields $\Gamma_0(T) \propto \rho(T)$. This seems sensible since the proportionality holds for the A_{1g} results in the entire temperature range above T_{SDW} and for the B_{1g} spectra above T_f. Fig. S8 shows the steps and checks necessary for the procedure. The analytical function used reads

$$\chi''_{\mathrm{cont}}(\Omega,T) = [\alpha_1 + \alpha_2 \cdot T] \tanh\left(\frac{\Omega}{\tilde{\Gamma}_0(T)}\right) + [\beta_1 + \beta_2 \cdot T]\left(\frac{\Omega}{\tilde{\Gamma}_0(T)}\right) \tag{S5}$$

which obeys $\chi''_{\mathrm{cont}}(-\Omega,T) = -\chi''_{\mathrm{cont}}(\Omega,T)$ as required by causality. α_1, α_2, β_1 and β_2 depend only on doping x. For $x = 0.025$ we used $\alpha_1 = 0.82379$, $\alpha_2 = -0.00138$, $\beta_1 = -0.00923$, and $\beta_2 = 0.00028$. $\tilde{\Gamma}_0(T)$ is a fitting parameter that is selected in a way that the inverse slope $\Gamma_c(0,T)$ of $\chi''_{\mathrm{cont}}(\Omega,T)$ follows the resistivity (orange diamonds in Fig. S8 d). If a constant continuum is used the fluctuations can be isolated in a qualitatively similar fashion. However, the experimental data in Fig. 2 vary more slowly close to T_s.

Below T_s the uncertainties increase since surface layers accumulate rapidly in the presence of twin boundaries where the surface assumes a more polar character. This can be seen directly in Fig. S1 c.

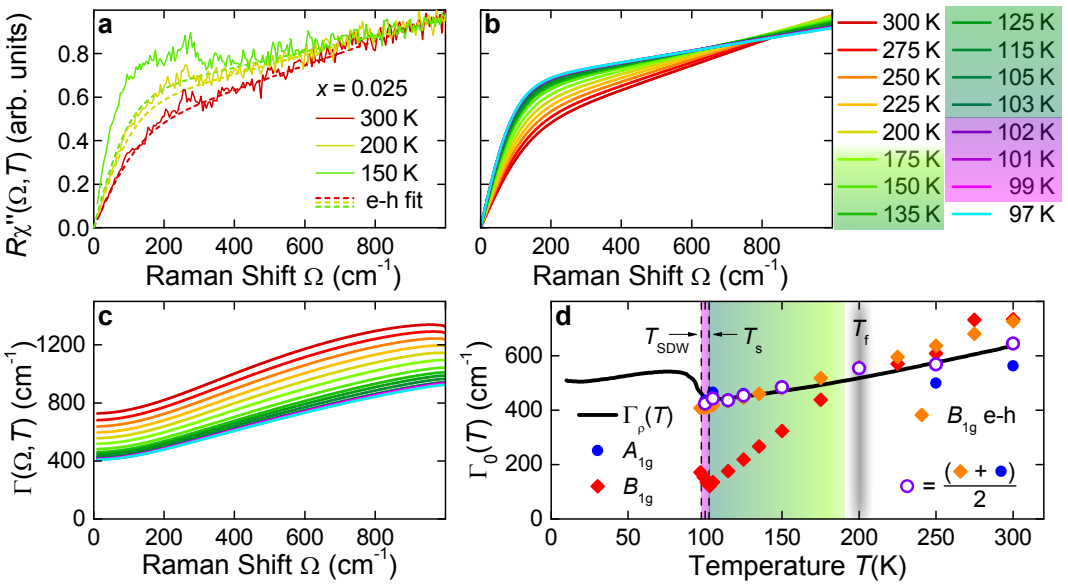

FIG. S8. Determination of the e-h continuum and subtraction from the full response in $Ba(Fe_{1-x}Co_x)_2As_2$ (x = 0.025). **a** The analytical function (red dashes) provides a reasonable fit at 300 K. At lower temperatures the fluctuations emerge above the continuum and the analytical functions lie below the data (yellow and green dashes). **b** The analytical model is varied so as to reproduce the temperature dependence of the resistivity as shown as orange diamonds in panel **d**. **c** Dynamical relaxation rates $\Gamma(\Omega,T)$ derived from the synthetic spectra in panel **b**. The zero-energy extrapolation values of $\Gamma_c(0,T)$ are plotted as orange diamonds in **d**. The A_{1g} and B_{1g} data are taken from Fig. 2.

[1] Chauvière, L. *et al.* Doping dependence of the lattice dynamics in $Ba(Fe_{1-x}Co_x)_2As_2$ studied by Raman spectroscopy. *Phys. Rev. B* **80**, 094504 (2009).

[2] Miller, P. B. & Axe, J. D. Internal Strain and Raman-Active Vibrations in Solids. *Phys. Rev.* **163**, 924–926 (1967).

[3] Chu, J.-H., Analytis, J. G., Kucharczyk, C. & Fisher, I. R. Determination of the phase diagram of the electron-doped superconductor $Ba(Fe_{1-x}Co_x)_2As_2$. *Phys. Rev. B* **79**, 014506 (2009).

[4] Chauvière, L. *et al.* Impact of the spin-density-wave order on the superconducting gap of $Ba(Fe_{1-x}Co_x)_2As_2$. *Phys. Rev. B* **82**, 180521 (2010).

[5] Sugai, S. *et al.* Spin-Density-Wave Gap with Dirac Nodes and Two-Magnon Raman Scattering

DOI: 10.1038/NPHYS3634

in $BaFe_2As_2$. *J. Phys. Soc. Japan* **81**, 024718 (2012).

[6] Gallais, Y. *et al.* Observation of Incipient Charge Nematicity in $Ba(Fe_{1-x}Co_x)_2As_2$. *Phys. Rev. Lett.* **111**, 267001 (2013).

[7] Böhmer, A. E. *et al.* Nematic Susceptibility of Hole-Doped and Electron-Doped $BaFe_2As_2$ Iron-Based Superconductors from Shear Modulus Measurements. *Phys. Rev. Lett.* **112**, 047001 (2014).

[8] Zawadowski, A. & Cardona, M. Theory of Raman scattering on normal metals with impurities. *Phys. Rev. B* **42**, 10732 (1990).

[9] Götze, W. & Wölfle, P. Homogeneous Dynamical Conductivity of Simple Metals. *Phys. Rev. B* **6**, 1226 (1972).

[10] Allen, J. W. & Mikkelsen, J. C. Optical properties of CrSb, MnSb, NiSb, and NiAs. *Phys. Rev. B* **15**, 2952–2960 (1977).

[11] Opel, M. *et al.* Carrier relaxation, pseudogap, and superconducting gap in high-T_c cuprates: A Raman scattering study. *Phys. Rev. B* **61**, 9752–9774 (2000).

[12] Drechsler, S.-L. *et al.* Insight into the physics of Fe-pnictides from optical and $T = 0$ penetration depth data. *Physica C (Amsterdam)* **470**, S332 – S333 (2010). Proceedings of the 9^{th} International Conference on Materials and Mechanisms of Superconductivity.

[13] Caprara, S., Di Castro, C., Grilli, M. & Suppa, D. Charge-Fluctuation Contribution to the Raman Response in Superconducting Cuprates. *Phys. Rev. Lett.* **95**, 117004 (2005).

[14] Karahasanovic, U. *et al.* Manifestation of nematic degrees of freedom in the raman response function of iron pnictides. *Phys. Rev. B* **92**, 075134 (2015).

[15] Venturini, F., Michelucci, U., Devereaux, T. P. & Kampf, A. P. Collective spin fluctuation mode and Raman scattering in superconducting cuprates. *Phys. Rev. B* **62**, 15204–15207 (2000).

[16] Caprara, S. *et al.* Signatures of nematic quantum critical fluctuations in the Raman spectra of lightly doped cuprates. *Phys. Rev. B* **91**, 205115 (2015).

[17] Paul, I. Nesting-induced large magnetoelasticity in the iron-arsenide systems. *Phys. Rev. B* **90**, 115102 (2014).

[18] Graser, S. *et al.* Spin fluctuations and superconductivity in a three-dimensional tight-binding model for $BaFe_2As_2$. *Phys. Rev. B* **81**, 214503 (2010).

[19] Devereaux, T. P. & Hackl, R. Inelastic light scattering from correlated electrons. *Rev. Mod. Phys.* **79**, 175 (2007).

[20] Mazin, I. I. *et al.* Pinpointing gap minima in $Ba(Fe_{0.94}Co_{0.06})_2As_2$ via band-structure calculations and electronic Raman scattering. *Phys. Rev. B* **82**, 180502 (2010).

[21] Muschler, B. *et al.* Band- and momentum-dependent electron dynamics in superconducting $Ba(Fe_{1-x}Co_x)_2As_2$ as seen via electronic Raman scattering. *Phys. Rev. B* **80**, 180510 (2009).

[22] Inosov, D. S. *et al.* Normal-state spin dynamics and temperature-dependent spin-resonance energy in optimally doped $BaFe_{1.85}Co_{0.15}As_2$. *Nat. Phys.* **6**, 178 (2010).

[23] Kuo, H.-H., Chu, J.-H., Kivelson, S. A. & Fisher, I. R. Ubiquitous signatures of nematic quantum criticality in optimally doped Fe-based superconductors. *ArXiv e-prints* (2015). 1503.00402.

[24] Eiter, H.-M. *et al.* Alternative route to charge density wave formation in multiband systems. *Proc. Nat. Acad. Sciences* **110**, 64–69 (2013).

[25] Tassini, L. *et al.* Dynamical Properties of Charged Stripes in $La_{2-x}Sr_xCuO_4$. *Phys. Rev. Lett.* **95**, 117002 (2005).